

Supplementary Tables

Table 1S; Strains used for genomic analysis (strains are congenic with W303)

Strain	Analysis	Genotype
DY150	RNA, MNase	<i>MATa ade2 can1 his3 leu2 trp1 ura3</i>
DY12554	RNA, MNase	<i>MATa ade2 can1 his3 leu2 lys2 trp1 ura3 pob3(Q308K)::KanMX</i>
DY16281	RNA, MNase	<i>MATa ade2 can1 his3 leu2 trp1 ura3 HHT1(K56Q) HHT2(K56Q)</i>
DY16302	RNA	<i>MATa ade2 can1 his3 leu2 trp1 ura3 HHT1(K56R) HHT2(K56R)</i>
DY16592	RNA, MNase	<i>MATa ade2 can1 his3 leu2 lys2 trp1 ura3 HHT1(K56Q) HHT2(K56Q) pob3(Q308K)::KanMX</i>
8159-4-1	RNA	<i>MATa ade2 can1 his3 leu2 trp1 ura3 spt16(G132D)</i>
8315-8-1	RNA	<i>MATa ade2 can1 his3 leu2 trp1 ura3 spt16-11</i>

Table 2S; Strains used for phenotype analysis in Figure 2 (strains are congenic with W303)

Strain	Genotype
Fig 2A, top	
DY150	<i>MATa ade2 can1 his3 leu2 trp1 ura3</i>
DY16281	<i>MATa ade2 can1 his3 leu2 trp1 ura3 HHT1(K56Q) HHT2(K56Q)</i>
DY16302	<i>MATa ade2 can1 his3 leu2 trp1 ura3 HHT1(K56R) HHT2(K56R)</i>
DY16313	<i>MATa ade2 can1 his3 leu2 lys2 trp1 ura3 HHT1(K56A) HHT2(K56A)</i>
DY12554	<i>MATa ade2 can1 his3 leu2 lys2 trp1 ura3 pob3(Q308K)::KanMX</i>
DY16592	<i>MATa ade2 can1 his3 leu2 lys2 trp1 ura3 HHT1(K56Q) HHT2(K56Q) pob3(Q308K)::KanMX</i>
DY16689	<i>MATa ade2 can1 his3 leu2 trp1 ura3 HHT1(K56R) HHT2(K56R) pob3(Q308K)::KanMX</i>
DY17970	<i>MATa ade2 can1 his3 leu2 met15 trp1 ura3 HHT1(K56A) HHT2(K56A) pob3(Q308K)::KanMX</i>
Fig 2A, bottom	
DY150	<i>MATa ade2 can1 his3 leu2 trp1 ura3</i>
DY16281	<i>MATa ade2 can1 his3 leu2 trp1 ura3 HHT1(K56Q) HHT2(K56Q)</i>
DY16302	<i>MATa ade2 can1 his3 leu2 trp1 ura3 HHT1(K56R) HHT2(K56R)</i>
DY7815	<i>MATa ade2 can1 his3 leu2 lys2 trp1 ura3 spt16-11</i>
DY17550	<i>MATa ade2 can1 his3 leu2 lys2 trp1 ura3 HHT1(K56Q) HHT2(K56Q) spt16-11</i>
DY17552	<i>MATa ade2 can1 his3 leu2 met15 ura3 HHT1(K56R) HHT2(K56R) spt16-11</i>
Fig 2B	
DY150	<i>MATa ade2 can1 his3 leu2 trp1 ura3</i>
DY16264	<i>MATa ade2 can1 his3 leu2 trp1 ura3 hst3Δ:HIS3 hst4Δ:KANMX</i>
DY19125	<i>MATa ade2 can1 his3 leu2 lys2 met15 trp1 ura3 pob3(Q308K):LEU2</i>
DY18250	<i>MATa ade2 can1 his3 leu2 trp1 ura3 pob3(Q308K):LEU2 hst3Δ:HIS3 hst4Δ:KanMX</i>
DY18243	<i>MATa ade2 can1 his3 leu2 trp1 ura3 lys2-128Δ</i>
DY18246	<i>MATa ade2 can1 his3 leu2 trp1 ura3 lys2-128Δ hst3Δ:HIS3 hst4Δ:KanMX</i>
10034-6-2	<i>MATa ade2 can1 his3 leu2 trp1 ura3 lys2-128Δ spt16-11</i>
10034-10-3	<i>MATa ade2 can1 his3 leu2 trp1 ura3 lys2-128Δ hst3Δ:HIS3 hst4Δ:KanMX spt16-11</i>
Fig 2C	
DY18243	<i>MATa ade2 can1 his3 leu2 trp1 ura3 lys2-128Δ</i>
10035-3-3	<i>MATa ade2 can1 his3 leu2 trp1 ura3 lys2-128Δ rtt109Δ(::KanMX)</i>
DY18247	<i>MATa ade2 can1 his3 leu2 trp1 ura3 lys2-128Δ pob3(Q308K):LEU2</i>

DY19131	<i>MATa ade2 can1 his3 leu2 trp1 ura3 lys2-128Δ pob3(Q308K):LEU2 rtt109:KanMX</i>
10034-6-2	<i>MATa ade2 can1 his3 leu2 trp1 ura3 lys2-128Δ spt16-11</i>
10035-6-4	<i>MATα ade2 can1 his3 leu2 trp1 ura3 lys2-128Δ rtt109-Δ(::KanMX) spt16-11</i>

Table 3S; Strains used in Supplemental Figure 1SC, H3 western blot (congenic with W303)

Strain	Genotype
DY5699	<i>MATa ade2 can1 his3 leu2 lys2 met15 trp1 ura3</i>
DY12949	<i>MATa ade2 can1 his3 leu2 lys2 met15 trp1 ura3 asf1::KanMX</i>
DY13030	<i>MATa ade2 can1 his3 leu2 lys2 trp1 ura3 rtt109::KanMX</i>
DY16281	<i>MATa ade2 can1 his3 leu2 trp1 ura3 HHT1(K56Q) HHT2(K56Q)</i>
DY16302	<i>MATa ade2 can1 his3 leu2 trp1 ura3 HHT1(K56R) HHT2(K56R)</i>
DY16313	<i>MATa ade2 can1 his3 leu2 lys2 trp1 ura3 HHT1(K56A) HHT2(K56A)</i>

Table 4S; primers used for detecting *HHT1* or *HHT2* mutations.

Name	Target	Sequence
F2899	HHT1	5'-GGTACTGTTGCTTTGAGAGAAATC
F3093	HHT1	5'-CTTGCAAGGCACCGATG
F2901	HHT2	5'-GTACTGTTGCCTTGAGAGAAATT
F2902	HHT2	5'-GATTCTTGCAAAGCACCGATA

Table 5S; Comparison of Spearman and Pearson correlation coefficients for scatter plots. Spearman and Pearson correlation coefficients were calculated in GraphPad Prism for scatter plots based on the genomic data presented here. Colors indicate the strength of the correlations, with negative values in shades of red and positive values in shades of green.

Correlations based on the log2FC mRNA (sense transcript signals; mutant/WT) for each genotype							Figure:
Versus:	<i>spt16-G132D</i>	<i>spt16-11</i>	<i>pob3-Q308K</i>	H3K56Q	H3K56R	H3K56Q <i>pob3-Q308K</i>	
log2 RNAPII ChIP signal/kb, Pelechano et al., 2010							
Spearman r	0.027	-0.090	-0.298	-0.147	-0.185	-0.356	3B, 3SB
Pearson r	-0.033	-0.107	-0.278	-0.167	-0.199	-0.368	
rlog2 mRNA (sense) WT, this study							
Spearman r	-0.100	-0.191	-0.353	-0.197	-0.222	-0.438	3C, 3SC
Pearson r	-0.144	-0.181	-0.299	-0.201	-0.196	-0.434	
log2 RNAPII ChIP signal/gene, Pelechano et al., 2010							
Spearman r	-0.054	-0.207	-0.255	-0.158	-0.177	-0.310	None
Pearson r	-0.079	-0.184	-0.243	-0.172	-0.182	-0.324	
log2 mRNA length bp							
Spearman r	-0.112	-0.159	0.003	-0.078	-0.018	-0.029	3D, 3SD
Pearson r	-0.101	-0.129	-0.014	-0.070	-0.010	-0.048	
log2 NET-seq signal Marquardt et al., 2014							
Spearman r	-0.088	-0.195	-0.197	-0.132	-0.156	-0.268	3SE
Pearson r	-0.082	-0.180	-0.174	-0.135	-0.147	-0.260	
log2 cDTA Synthesis Rate Sun et al., 2013							
Spearman r	0.096	-0.072	-0.276	-0.082	-0.159	-0.345	3SF
Pearson r	0.078	-0.062	-0.225	-0.105	-0.166	-0.336	
Correlations based on the log2FC (total RNA signals; mutant/WT) for each genotype							
log2 Total RNA WT (this study)							
Spearman r	-0.099	-0.199	-0.345	-0.257	-0.243	-0.419	None
Pearson r	-0.156	-0.214	-0.314	-0.273	-0.236	-0.453	
Correlations of rlog2FC (mRNA sense strand) for each mutant vs <i>pob3-Q308K</i>							
rlog2 mRNA (sense)							
Spearman r	0.304	0.656	1	0.557	0.623	0.765	4
Pearson r	0.346	0.663	1	0.607	0.620	0.743	
Correlations of rlog2FC (mRNA sense strand, slow growth signature removed) for each mutant vs <i>pob3-Q308K</i>							
rlog2 mRNA (sense), slow growth signature removed							
Spearman r	0.382	0.612	1	0.462	0.498	0.686	4SC
Pearson r	0.411	0.630	1	0.538	0.540	0.690	
Correlations based on changes in nucleosome occupancy							
	<i>pob3-Q308K</i>	H3K56Q	H3K56Q <i>pob3-Q308K</i>				
log2FC NDR Nuc occupancy vs log2FC mRNA							
Spearman r	-0.165	-0.178	-0.344				6
Pearson r	-0.197	-0.176	-0.342				
log2FC +1 Nuc Occupancy vs log2FC mRNA							
Spearman r	-0.113	-0.030	-0.068				6
Pearson r	-0.114	-0.035	-0.061				
log2FC Avg Gene Body Nuc Occupancy vs log2FC mRNA							
Spearman r	-0.184	-0.176	-0.231				6
Pearson r	-0.175	-0.168	-0.209				

Supplementary Figures

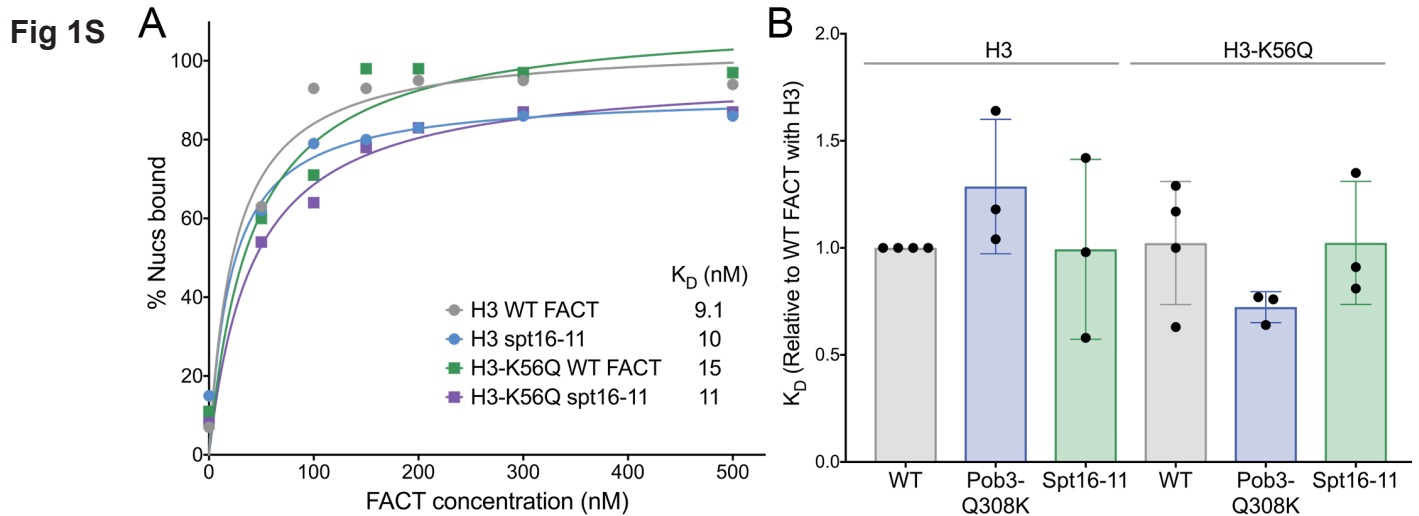


Figure 1S. Mutations of histone H3 did not strongly affect the affinity of FACT for nucleosomes.

(A) The affinities of either WT or mutant versions of FACT for nucleosomes constructed with either WT H3 or H3-K56Q were determined by electrophoretic mobility shift assays as described previously (XIN *et al.* 2009). K_D s were determined using GraphPad Prism to fit the binding data to a single-site binding model. Results from one experiment are shown for samples evaluated in parallel on the same gel with quantitation based on the H2B signal (Nucleosomes were labeled with Cy5 on the DNA and Oregon Green on H2B). (B) Multiple repeats of the assay in (A) were performed and K_D values obtained by quantitation of the DNA signal were normalized to the value for WT nucleosomes with WT FACT run in parallel on each gel to reduce the effects of variation among gels run on different days. The affinity of FACT with the Pob3-Q308K mutation for nucleosomes with the H3-K56Q mutation was slightly reduced (72% of WT, $P = 2.2\%$ in a paired t test) but none of the other combinations produced significant changes.

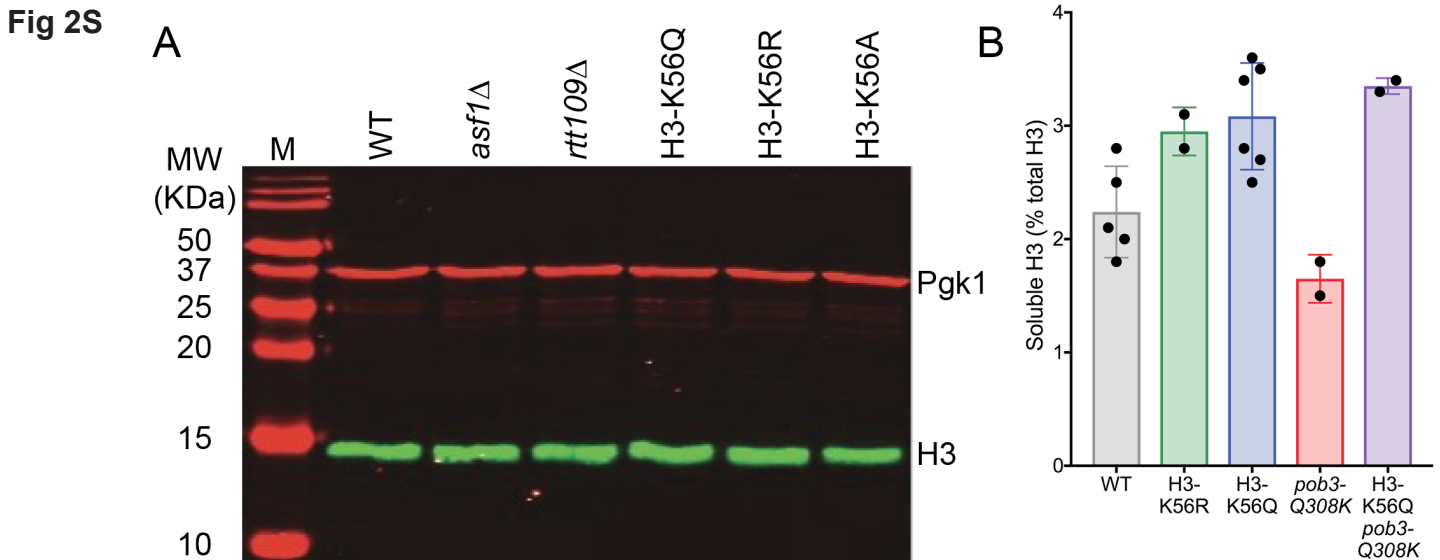


Figure 2S. Mutations of histone H3 did not strongly affect the level of H3 or its incorporation into chromatin.

(A) Strains (see Table 3S for full genotypes) were grown to log phase and proteins were extracted by the TCA method (McCULLOUGH *et al.* 2015). A western blot was prepared using 5 μ g of total protein from each strain, then the blot was probed with antibodies against histone H3 or Pgk1 as an additional loading control. Molecular weight standards with approximate sizes in kDa are shown (M, Li-Cor Odyssey One-Color). (B) Strains with the genotypes indicated (Table 1S) were tested for soluble and total histone H3 as described previously (McCULLOUGH *et al.* 2013). Briefly, cells were spheroplasted, lysed by hypotonic stress, then centrifuged to separate chromatin from soluble histones. The level of H3 in each fraction was then determined by quantitative western blotting using titrations of each fraction and a WT strain lysate to establish linearity of detection. The fraction of soluble H3-K56Q was 1.7-fold higher than WT ($P = 3.4\%$, paired t test) but the increase was less than 1% of the total H3 and was therefore considered negligible.

Figure 3SA. Principal-component analysis of $\log_2(\text{mRNA, sense})$ dataset.

Principal component analysis was performed in R on the independent replicates for the RNA-seq samples. The first two components, accounting for ~64% of the variance, are plotted for each strain.

Fig 3SA

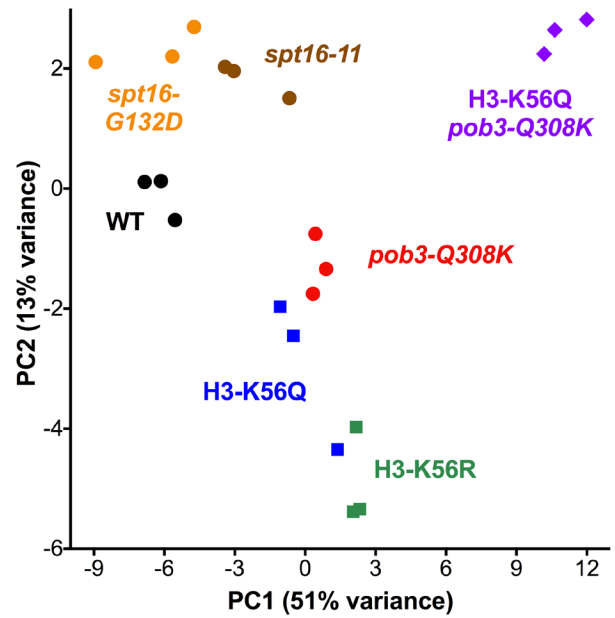


Fig 3SB

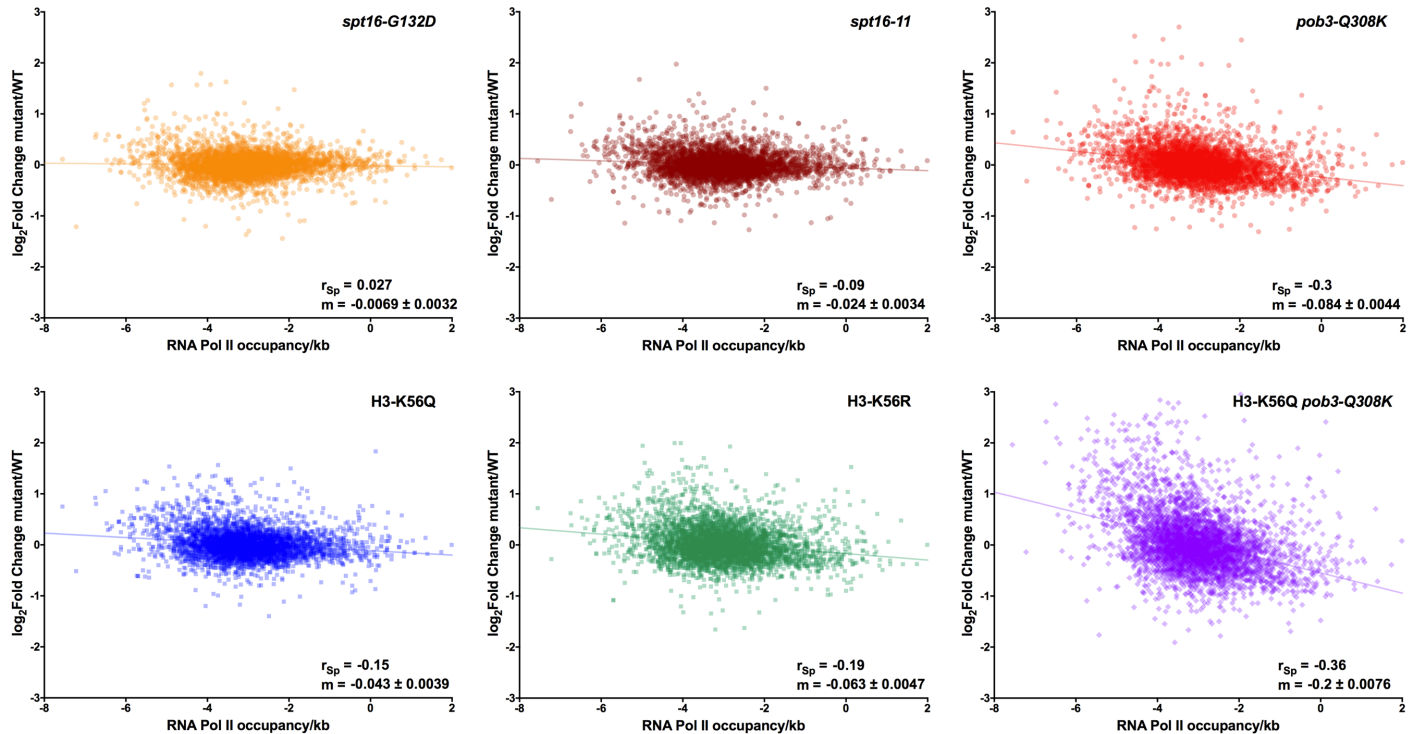


Figure 3SB-F. Comparisons of the change in transcript levels for all mutants to gene characteristics.

The $\log_2\text{FC}$ values for the RNA-seq data for each set of mutants was determined as in Fig 3 in the main text and plotted against different measurements of transcription frequency or the length of each transcription unit. (B) Transcription frequency is estimated as RNA Pol II occupancy measured by ChIP-seq (published by PELECHANO *et al.* 2010; the *pob3-Q308K* data shown here are the same as in Fig 3B). Spearman correlation coefficients and linear regression slopes are given for each scatter plot, and summarized in Table 5S. RNA Pol II occupancy, NET-seq, and comparative dynamic transcriptome analysis (cDTA) are expected to provide a more accurate picture of ongoing transcription in WT yeast cells, but our $\log_2\text{FC}$ data are derived from the steady-state level of transcripts and we noted that while many correlations were weak or moderate, they were consistently highest with our internal $\log_2(\text{mRNA, sense strand})$ data and derivatives of it.

Fig 3SC

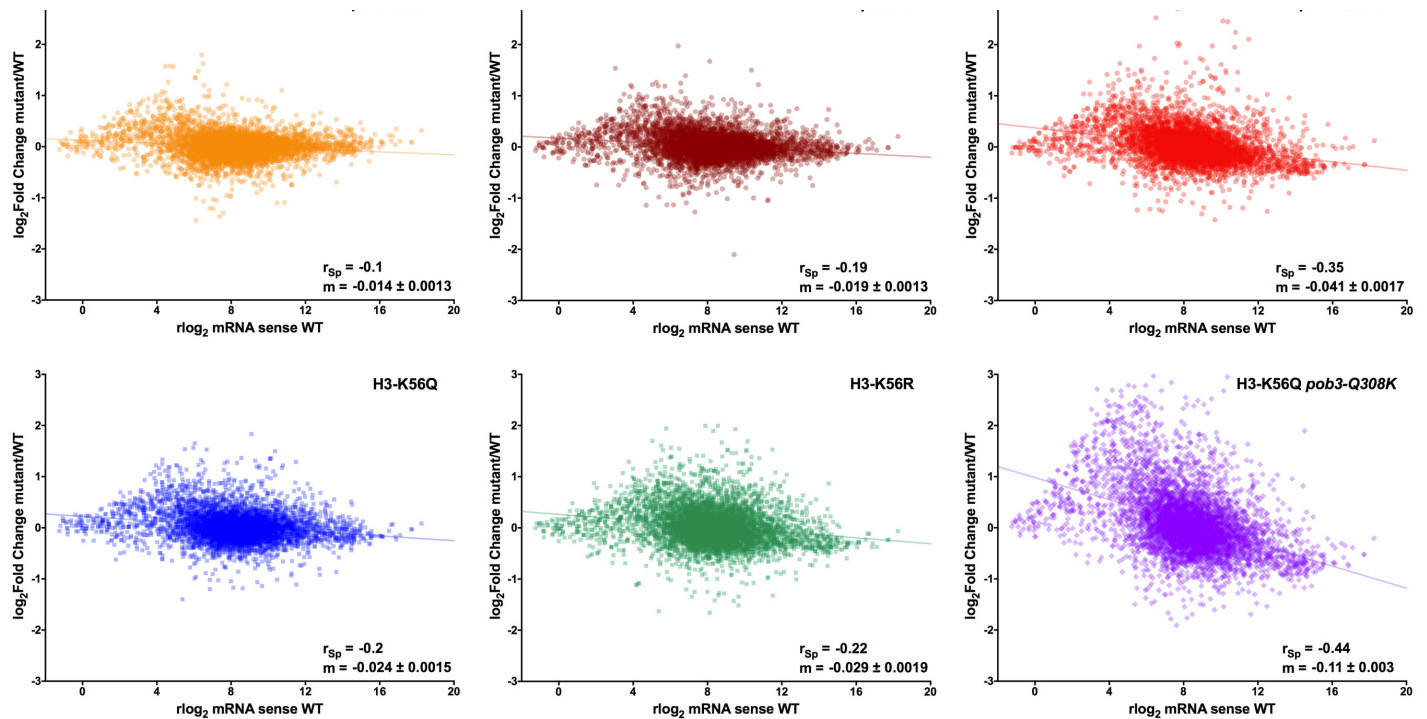


Fig 3SC. The \log_2 FC values for the RNA-seq data plotted against our $r\log_2$ data for the total mRNA (sense strand) from the WT strains (the *pob3-Q308K* data shown here are the same as in Fig 3C).

Fig 3SD

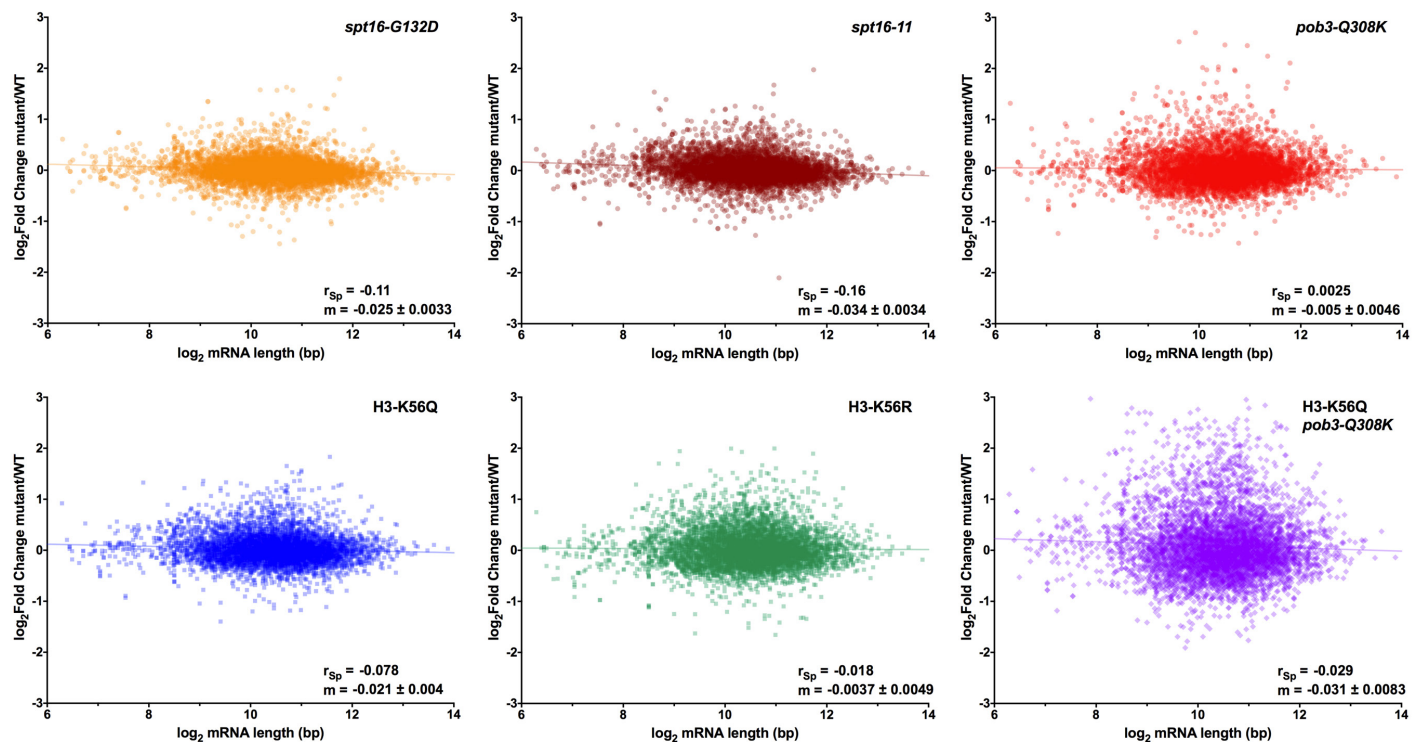


Fig 3SD. The \log_2 FC values for the RNA-seq data plotted against the annotated transcription unit lengths ((the *pob3-Q308K* data shown here are the same as in Fig 3D).

Fig 3SE

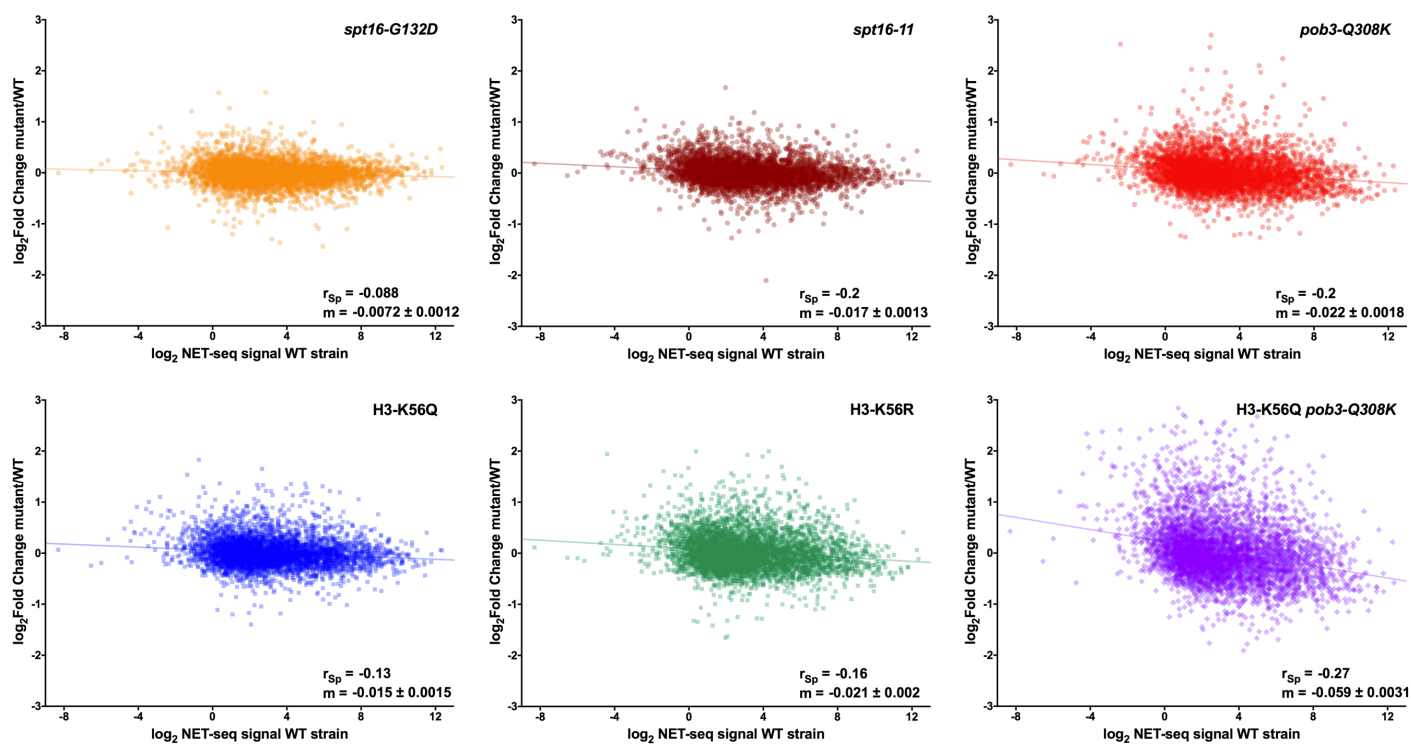


Figure 3SE. The \log_2 FC values for the RNA-seq data plotted against NET-seq results (MARQUARDT *et al.* 2014).

Fig 3SF

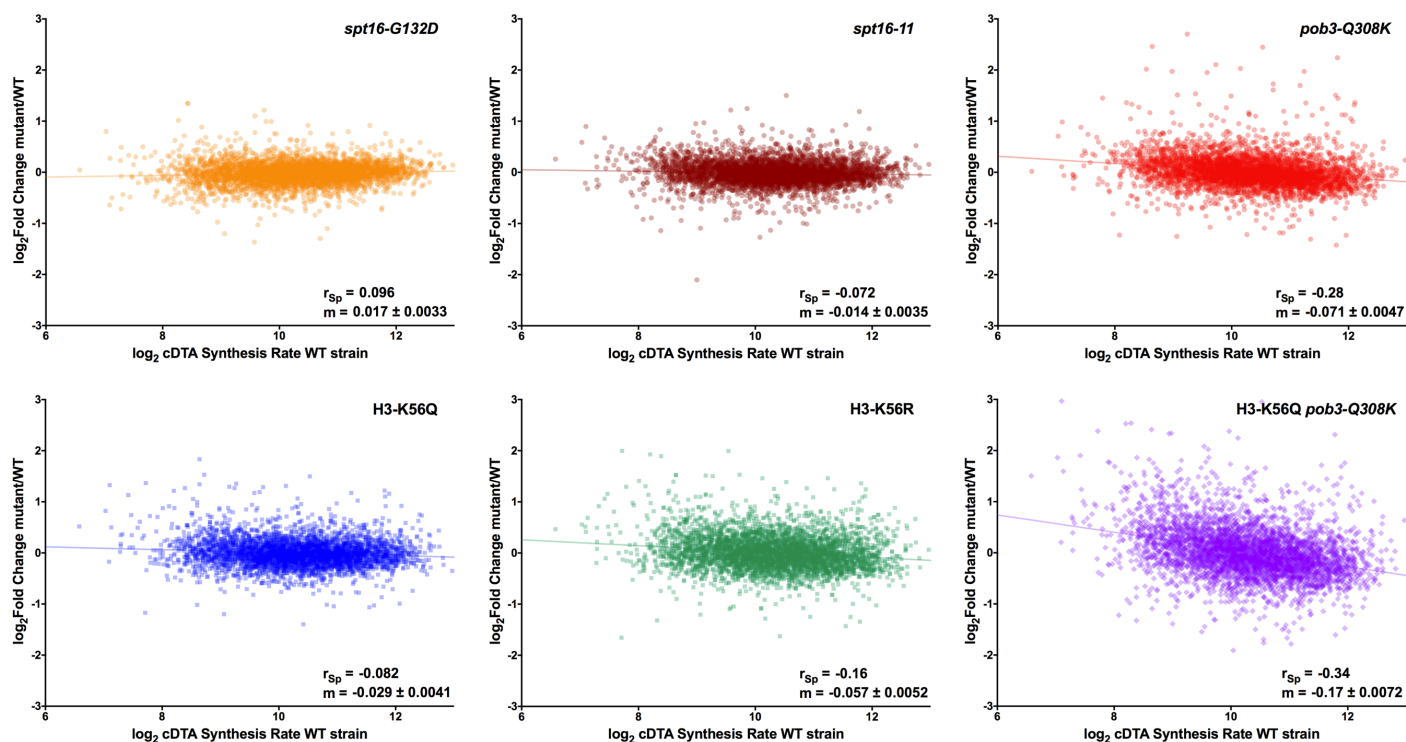


Figure 3SF. The \log_2 FC values for the RNA-seq data plotted against metabolic labeling or comparative dynamic transcriptome analysis (cDTA) synthesis rates (SUN *et al.* 2013).

Fig 3SG

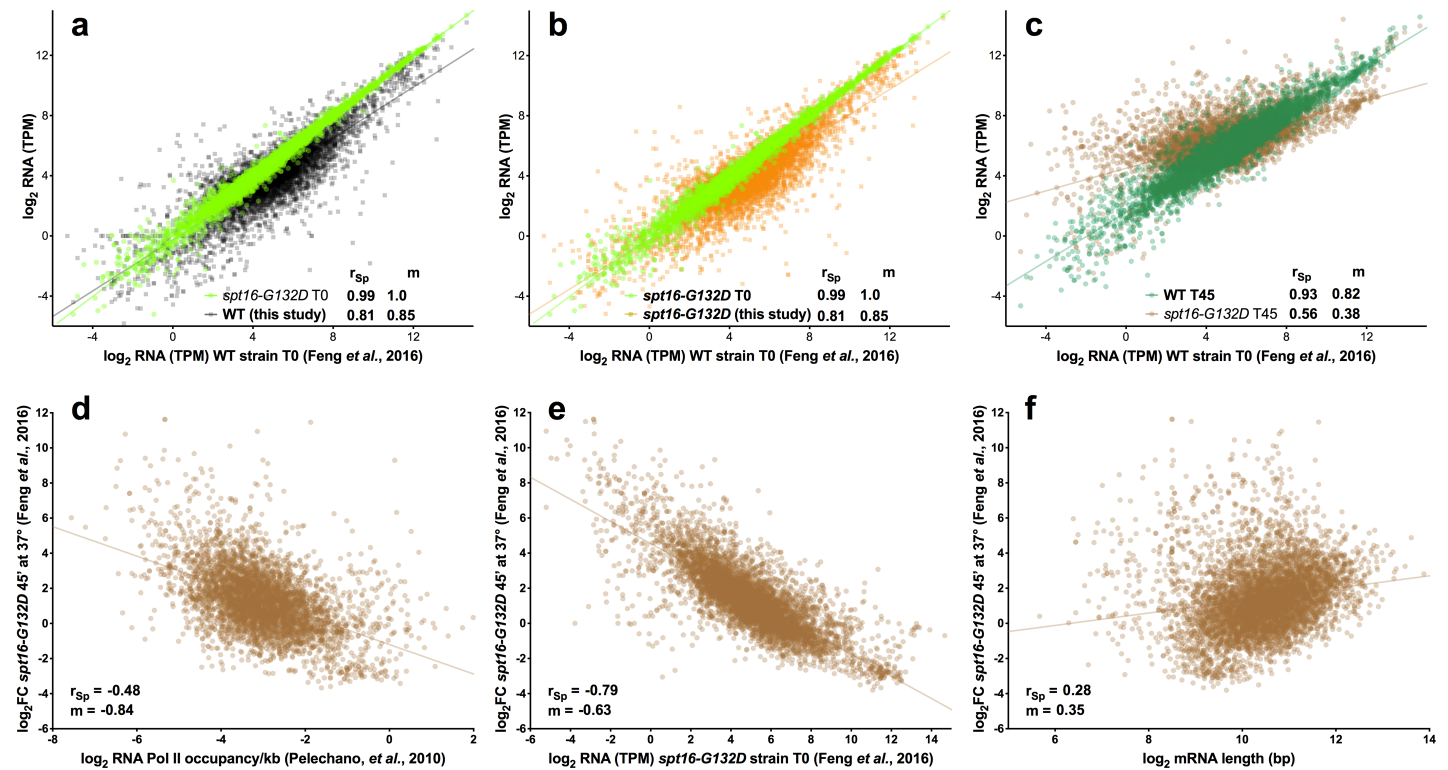
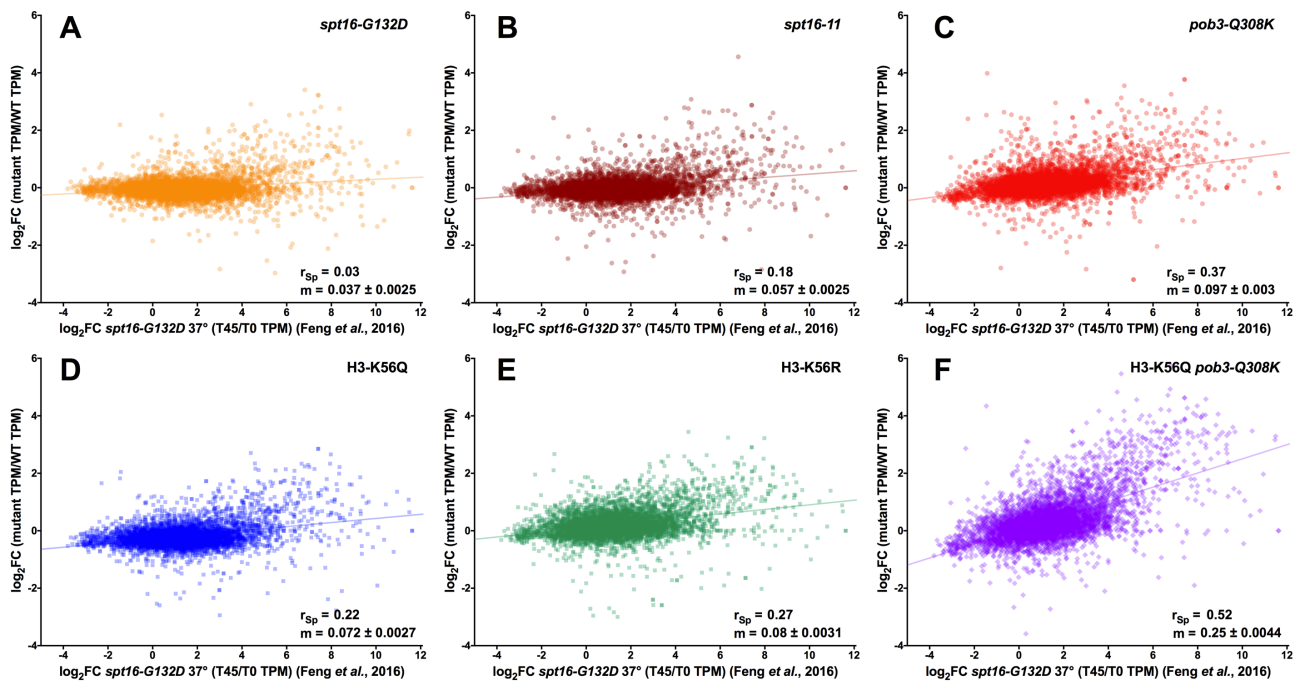
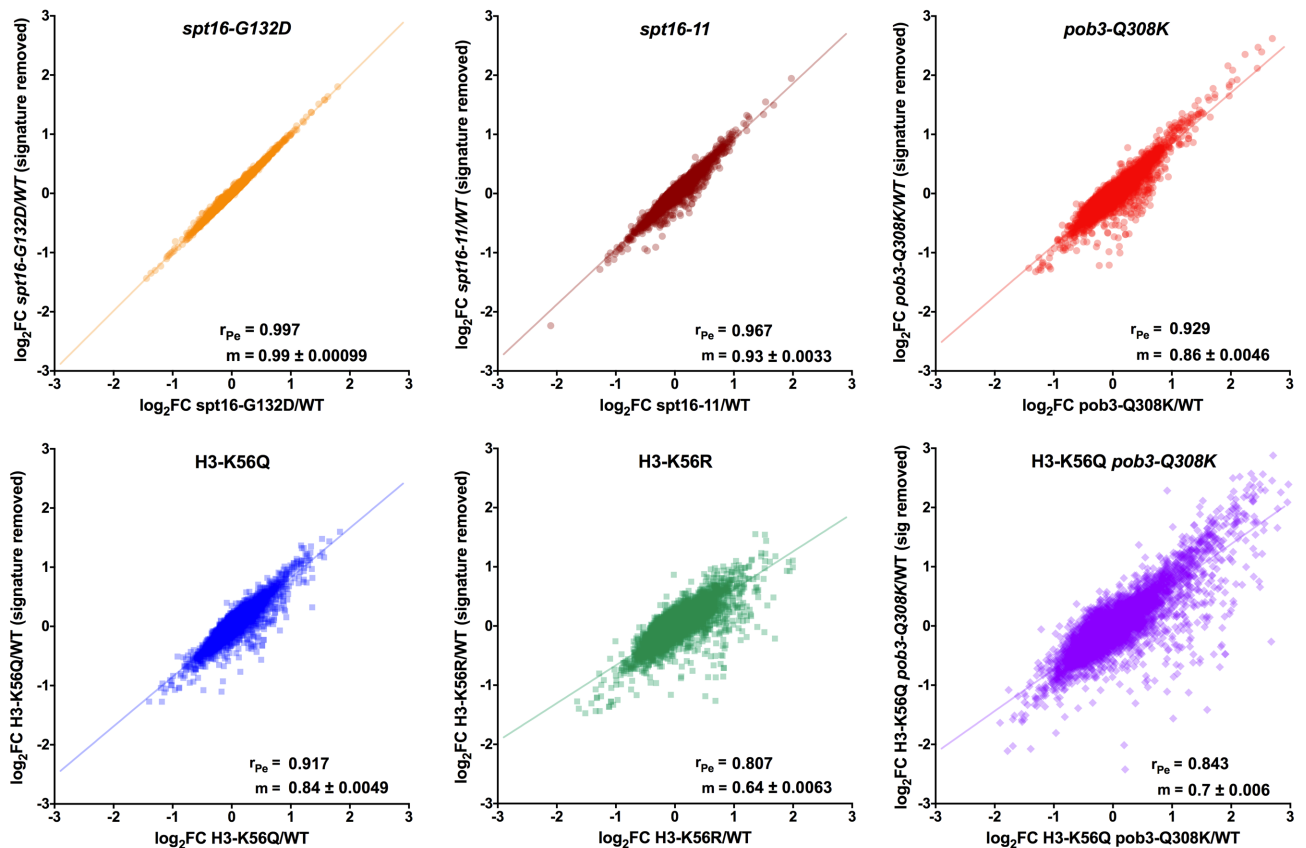


Figure 3SG. Comparison of the effects of chronic FACT or H3-K56 status mutations with acute withdrawal of FACT using published data (FENG *et al.* 2016).

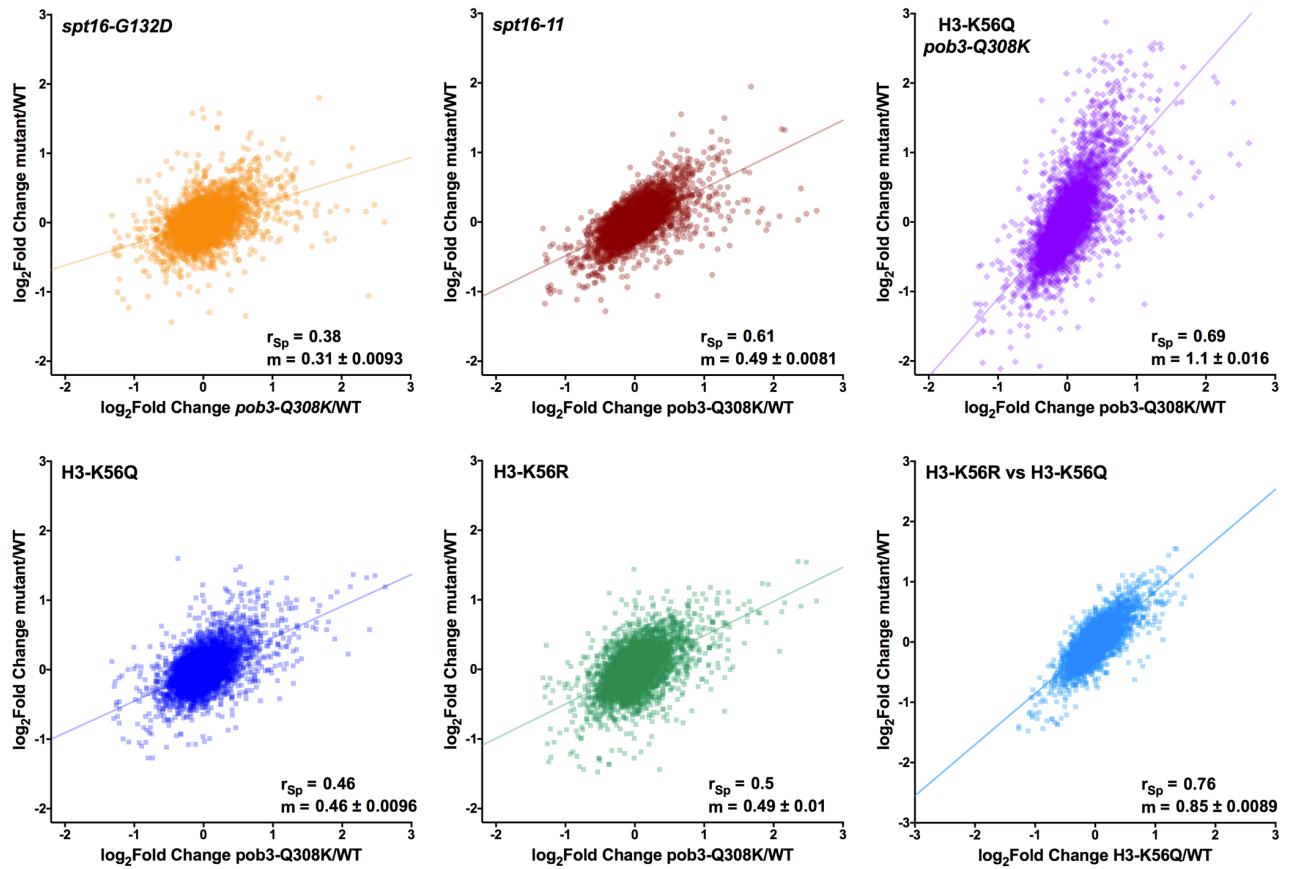
To ask how chronic exposure to non-lethal FACT or H3 mutations with specific functional defects compares with acute loss of FACT, we reanalyzed the data from FENG *et al.* 2016. These authors used a temperature sensitive allele, *spt16-G132D*, that causes rapid degradation of FACT to perform RNA-seq under permissive (25°) and restrictive (37°) conditions. We preferred this dataset to other similar published reports because it used a short (45 minute) exposure to the restrictive temperature to limit complications that could arise as cells experience lethal defects. As the dataset contained single samples for each condition, we reanalyzed it using the TPM normalization method (see the Supplemental Methods below). (a, b) The *spt16-G132D* mutant grown at 25° (T0) gave RNA-seq results that correlated very strongly with the WT strain grown in parallel ($r = 0.99$, $m = 1.0$), and our WT and *spt16-G132D* (grown at 30°) data also correlated well with the FENG *et al.* 2016 WT results ($r = 0.81$, $m = 0.85$ for both). Incubating the WT strain to 37° for 45' (T45) causes some changes in transcript levels globally, but *spt16-G132D* displays a much stronger effect, with notable “flattening” of the correlation (panel c, $r = 0.56$, $m = 0.38$), indicating a general increase in infrequently transcribed genes and a decrease in more abundant transcripts. Confirming this, direct comparison of the $\log_2 \text{FC}$ values (*spt16-G132D* T45/T0) vs RNA Pol II occupancy (panel d) or total normalized RNA (panel e), produced much stronger correlations than our chronic FACT mutation data. Notably, the same was not true of the comparison with transcription unit length (panel f). These outcomes suggest that acute withdrawal of FACT makes rapid cycling of initiation difficult, but does not directly affect elongation efficiency as strongly.

Fig 4SA**Figure 4SA.** Acute withdrawal of FACT affects transcript levels from individual genes differently than chronic mutations.

Whereas each of the mutant strains tested here caused similar effects at the same genes (Fig 4), a similar analysis comparing individual viable mutants to the effects of acute loss of FACT as measured by incubating an *spt16-G132D* strain for 45' at 37° (FENG *et al.* 2016) produced weaker correlations. The combination of H3-K56Q with *pob3-Q308K* gave a moderate correlation ($r_{Sp} = 0.52$, $m = 0.25$) suggesting that multiple hits at different points in the pathway promoted by the FACT:H3-K56 functional interaction started to have features of acute FACT withdrawal.

Fig 4SB**Figure 4SB-4SC.** Removing the “slow growth signature” had small, variable effects on the RNA-seq datasets.

The Holstege lab surveyed over 1000 deletion mutants by RNA-seq (O'DUIBHIR *et al.* 2014) and noted that many slow-growing strains had a common set of changes in transcript abundance that they associated with perturbed distribution of cells in populations among different phases of the cell cycle. We used the script

Fig 4SC

described by O'Duibhir *et al.* 2014 to subtract this signature from our data, with variable but small effects (Fig 4SB). The smallest effect was on *spt16-G132D*, as expected as this strain exhibits essentially normal growth at 30°. The largest effect was observed with the H3-K56R data, which was surprising given the small effect on growth at 30° observed with this strain (Fig 2A). Notably, removing the signature did not strongly affect the correlation between the \log_2 FC outcomes and transcript level, transcription frequency, or transcription unit length (not shown) or the pairwise correlations between mutants (Fig 4SC).

Fig 5SA

Fig 5SA. Principal Component analysis of MNase-seq sample replicates.

Principal component analysis was performed in R on the independent replicates for the MNase-seq samples. The first two components, accounting for ~83% of the variance, are plotted for each strain.

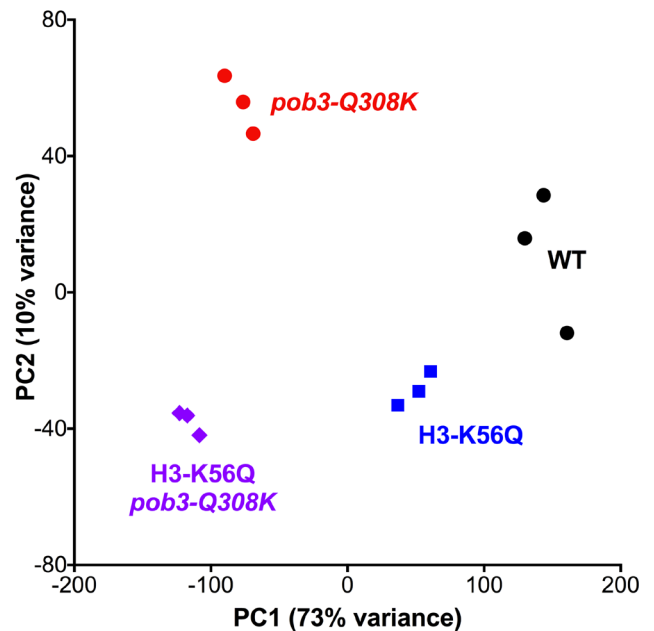


Fig 5SB

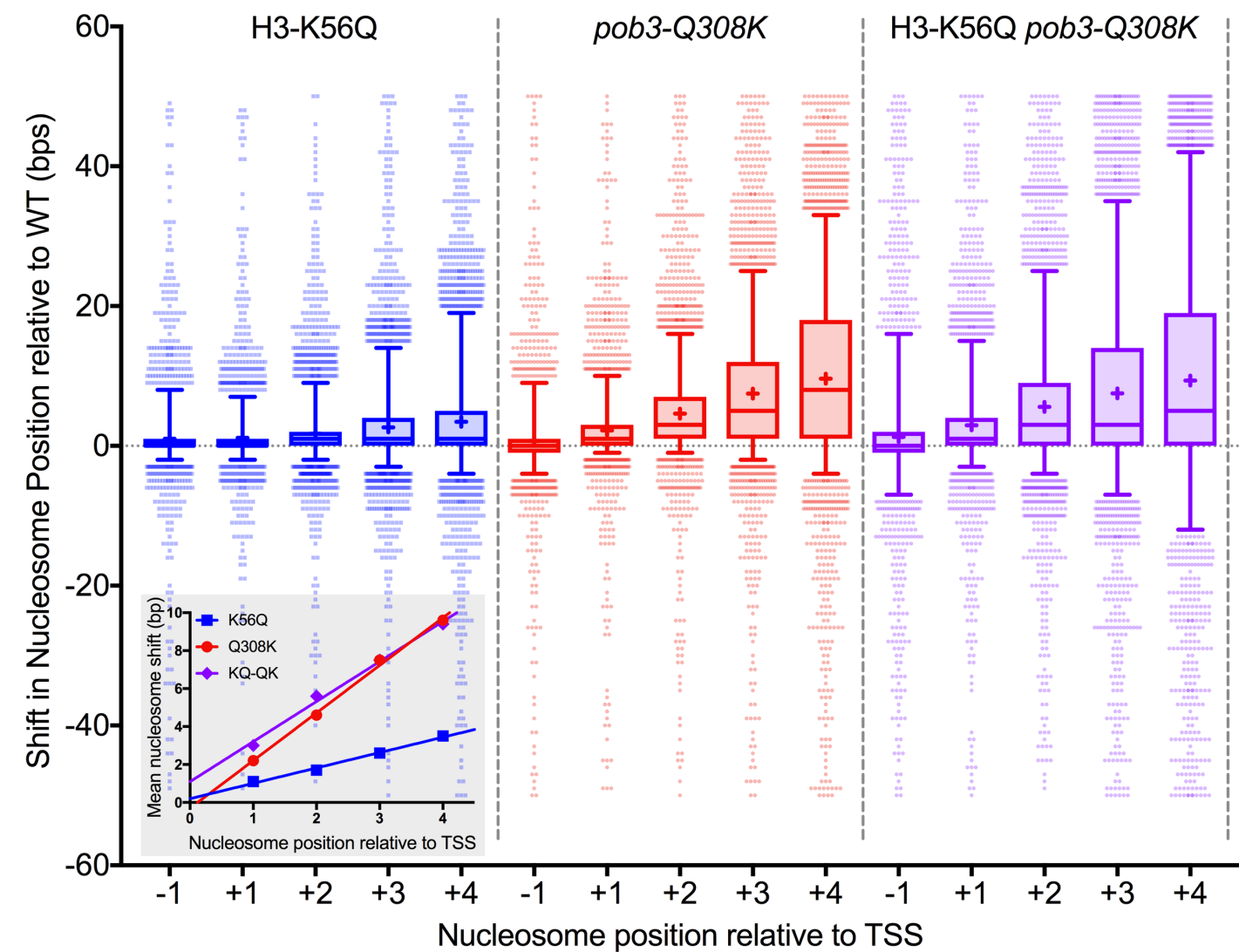


Fig 5SB. Analysis of nucleosome shifts in mutant strains. Nucleosome midpoints were called and aligned as in Fig 5A, then the change in each nucleosome position from the -1 to +4 positions relative to the TSS were estimated for each gene (see the Supplemental Materials and Methods for details) and displayed as a box and whisker plot. The box shows the 25th to 75th percentile with the median indicated by a horizontal line and the mean indicated by a “+” symbol, the whiskers show the 5th - 95th percentiles, and outliers are shown as symbols. The inset shows a plot of the mean values for each nucleosome for each mutant, showing a linear relationship, indicating that the changes are minimal at the -1 nucleosome, then the 3’ shift is cumulative with each nucleosome downstream of the TSS.

Fig 5SC

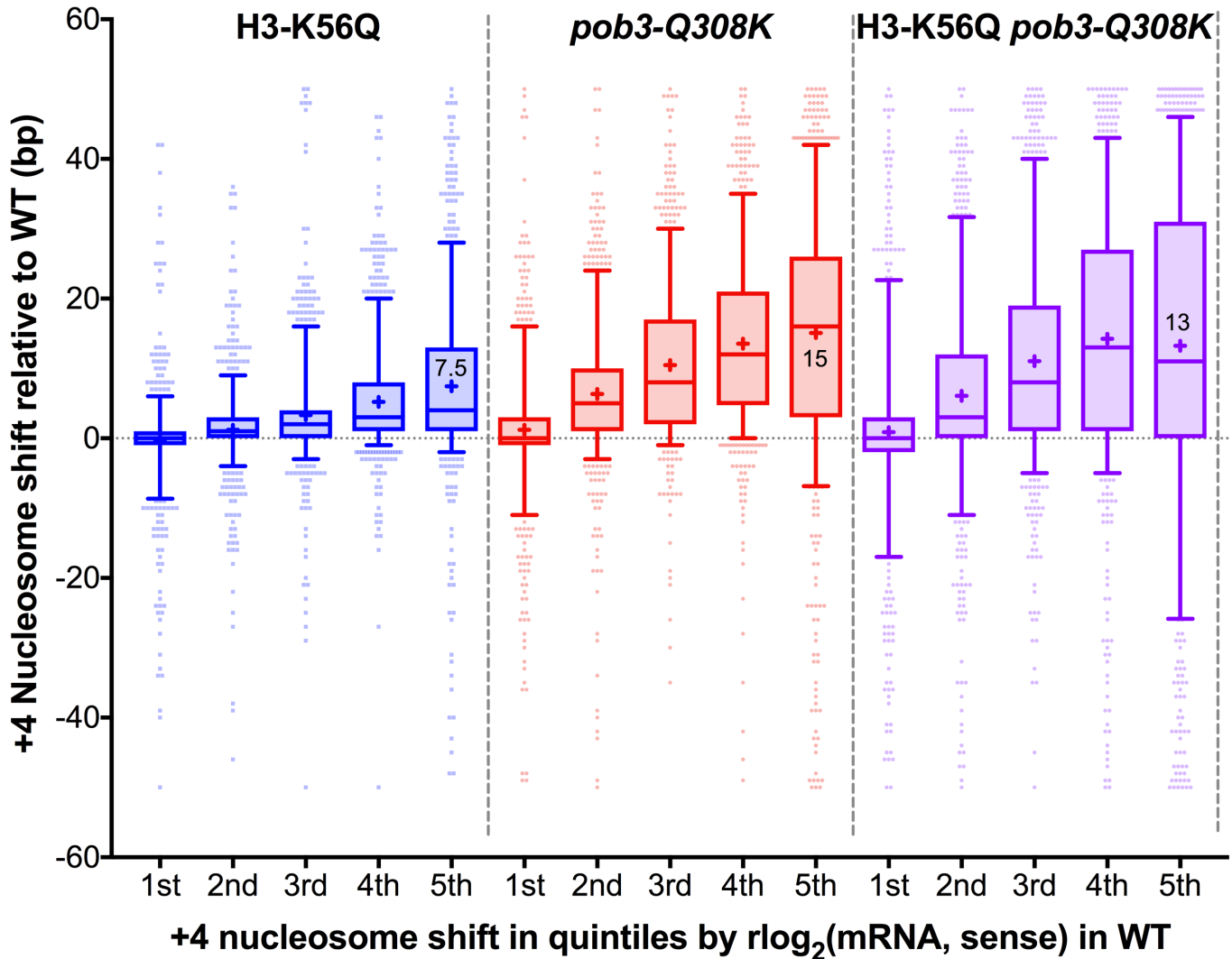


Fig 5SD

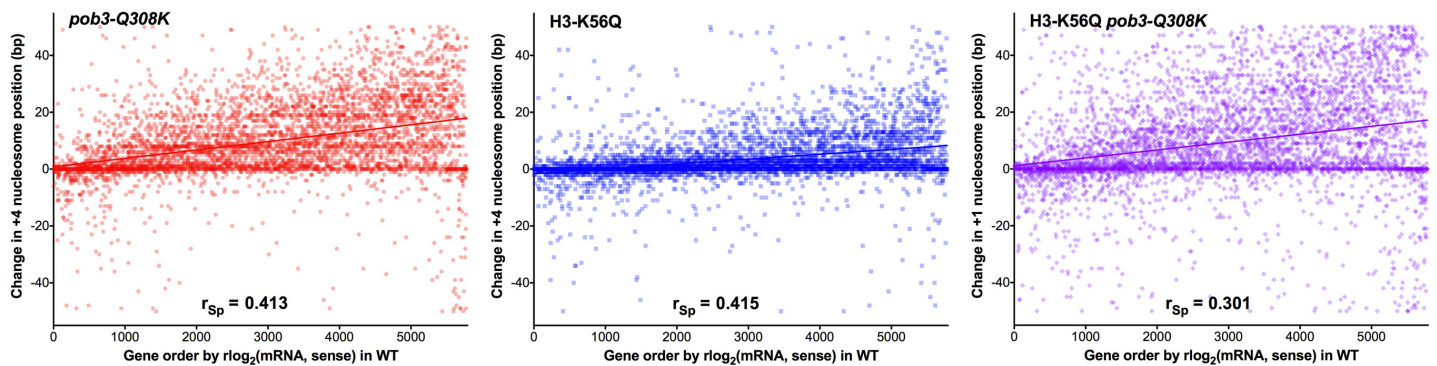


Fig 5SC, 5SD. The relationship between the shift in nucleosome position and the frequency of transcription. Genes were binned by quintiles from the lowest (1) to the highest (5) $\log_2(\text{mRNA, sense strand})$ values for the WT strain from this study, and box-whisker plots were generated as described above for the shift at the +4 nucleosome for each quintile for each mutant. This analysis shows a significantly higher shift in the +4 nucleosome for abundantly transcribed genes, suggesting a correlation between the nucleosome positioning shift and the frequency of transcription. This is partially supported by scatter plots comparing the shift in position of the +4 nucleosome with transcript abundance for each gene displayed by the order of abundance (low to high), which give moderate to low correlation values overall. We conclude that the method of estimating nucleosome position is noisy, and the correlation between nucleosome shift and transcription frequency is moderate, but there is a significant linkage between these factors.

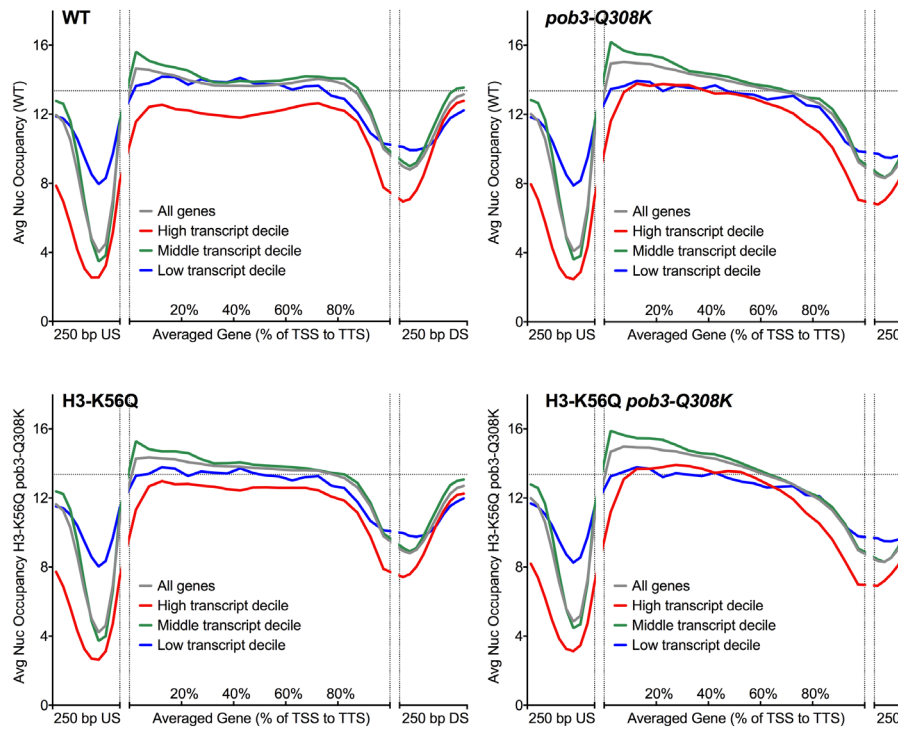
Fig 5SE

Fig 5SE, 5SF. A FACT mutant fails to maintain the normal low nucleosome occupancy observed in frequently transcribed genes.

(E) Average nucleosome occupancy normalized for gene length was plotted as in Fig 5B. Genes were parsed into deciles based on the $\log_2(\text{mRNA, sense strand})$ values for the WT strain from this study (1st-10th percentile is low, 45-55 is middle, 90-100 is high). The most frequently transcribed genes in the WT strain showed low nucleosome occupancy upstream, in the NDR, across the gene body, and downstream (red line). This effect was less prominent in the H3-K56Q strains (higher nucleosome occupancy for the frequently transcribed genes), and even less in *pob3-Q308K* mutants. To quantitate this, we calculated the average nucleosome occupancy in gene bodies. To avoid complications arising from the 5' end increase/3' end decrease in nucleosome occupancy noted in Figs 5B-D, we used only the central portion of the averaged gene (30% to 70% of the average transcription unit length). (F) The decile with the lowest abundance of transcripts showed small changes in a box-whisker plot generated as described above, but the decreased abundance in highly transcribed genes, and the loss of this feature in mutant strains, were supported by statistical analysis (unpaired t tests with the values indicated).

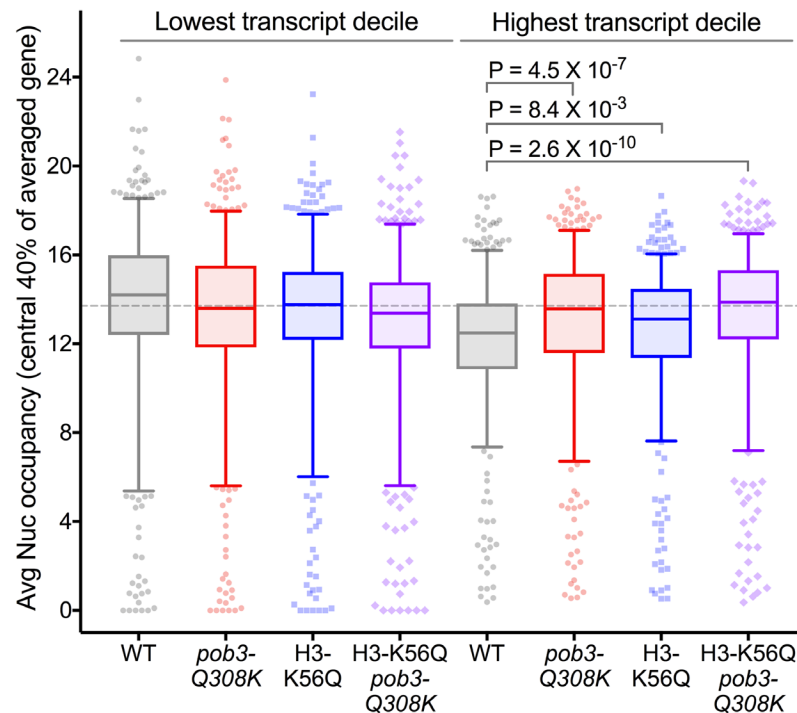
Fig 5SF

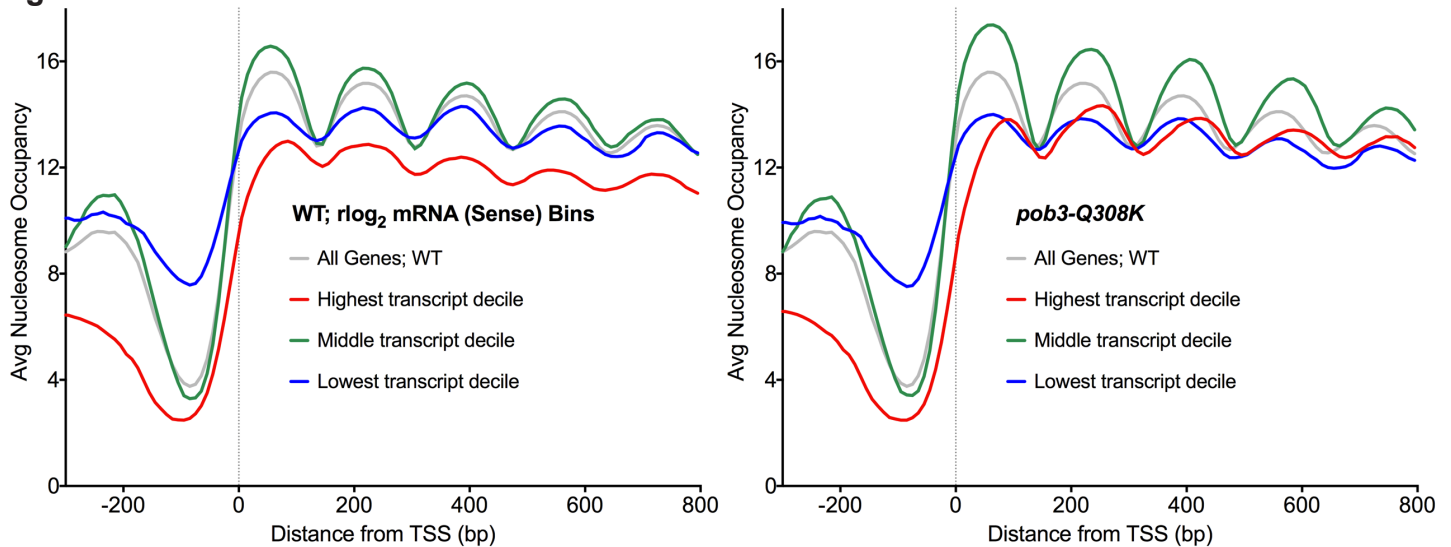
Fig 5SG

Fig 5SG. Increased nucleosome occupancy in frequently transcribed genes is visible without normalizing gene length.

Genes were binned into deciles as in Fig 5SE, but the average nucleosome occupancy was plotted for genes aligned by the TSS to ensure that the effects noted in Fig 5SE-F are not an artefact of normalization.

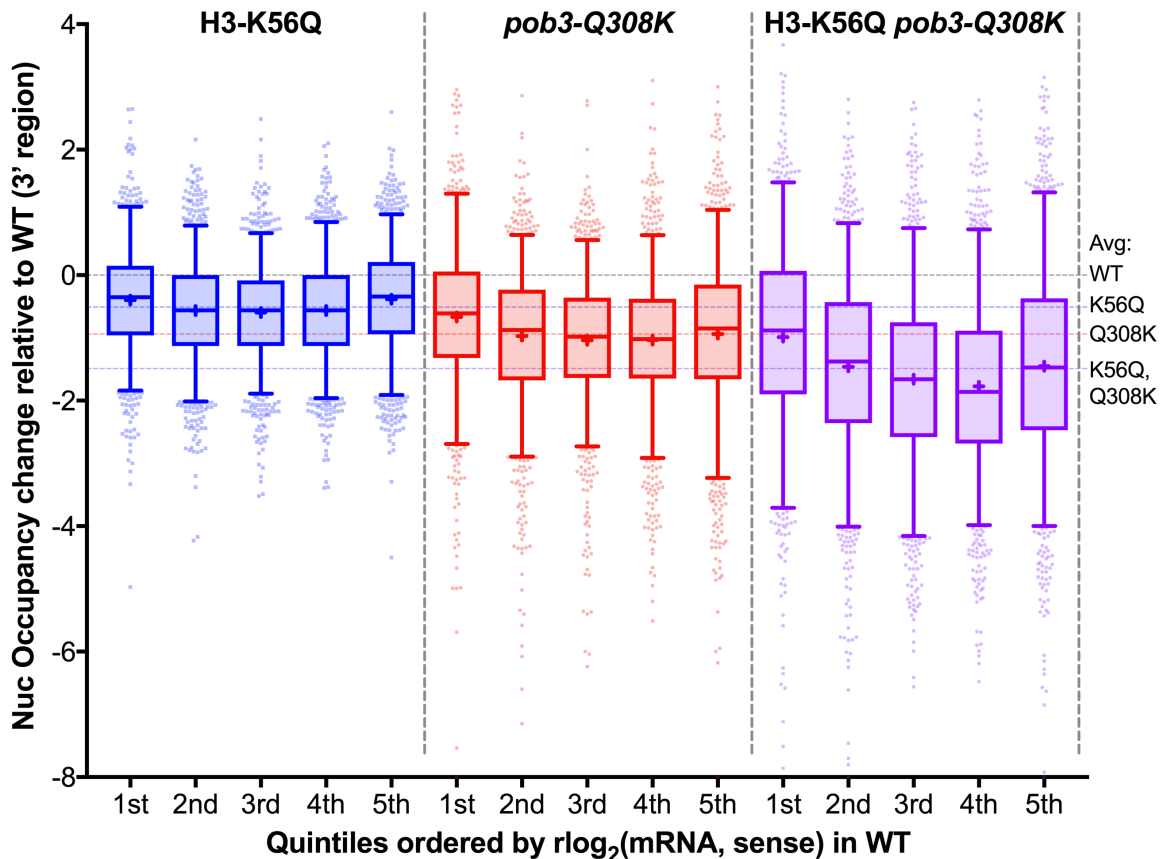
Fig 5SH

Fig 5SH. Effects of transcription frequency on 3' end nucleosome occupancy changes in mutants.

Average nucleosome occupancy was calculated as in Fig 5SE and binned into quintiles according to transcript abundance as in Fig 5SC, except that the region from 70% to 90% of the averaged gene was used to focus on the depopulation of nucleosomes over the 3' ends of genes. Box and whisker plots were generated with the features noted above (box is 25th-75th percentile, whiskers 5th to 95th percentile, + is the mean), with a dotted line indicating the overall average for each strain. All strains displayed the strongest decreases in nucleosome occupancy in the region tested in genes near the middle of the abundance spectrum, with diminished effects in genes with both the least and the most abundant transcripts. Transcription frequency and nucleosome depopulation therefore display a complex relationship.

Fig 5SI

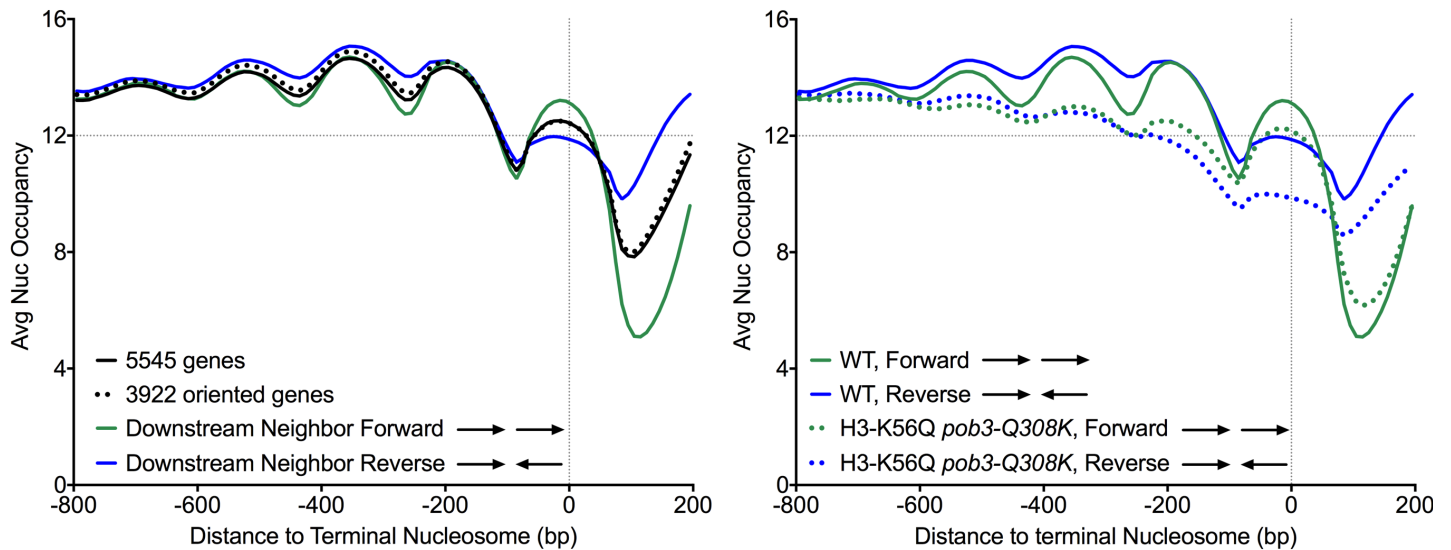
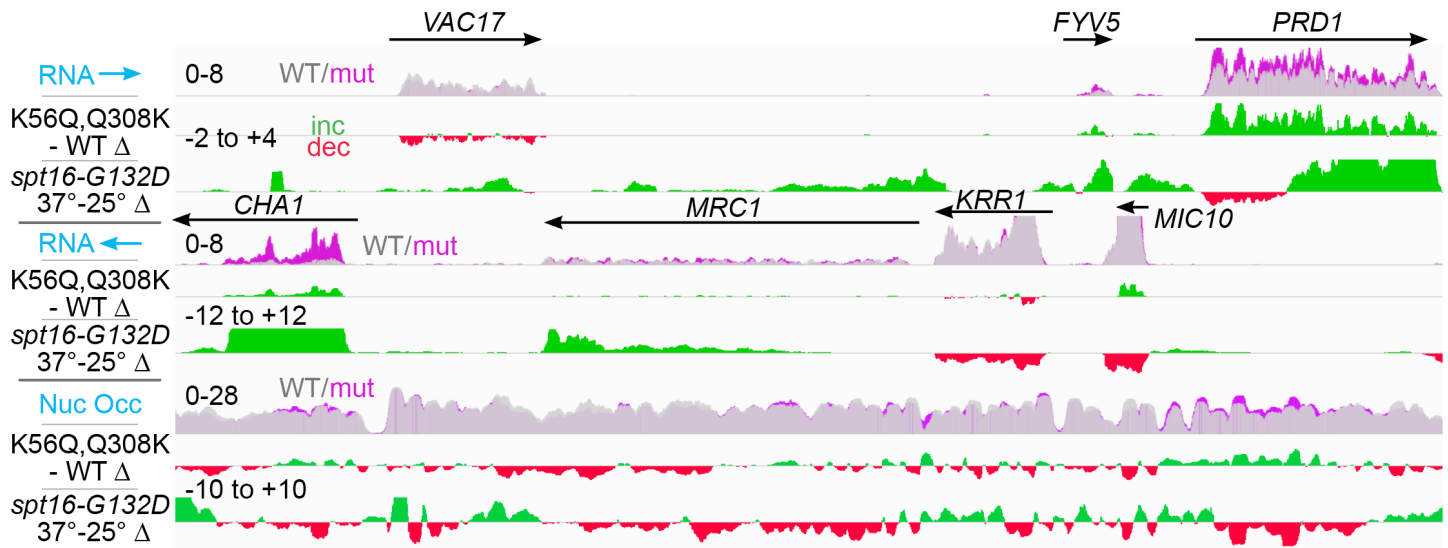


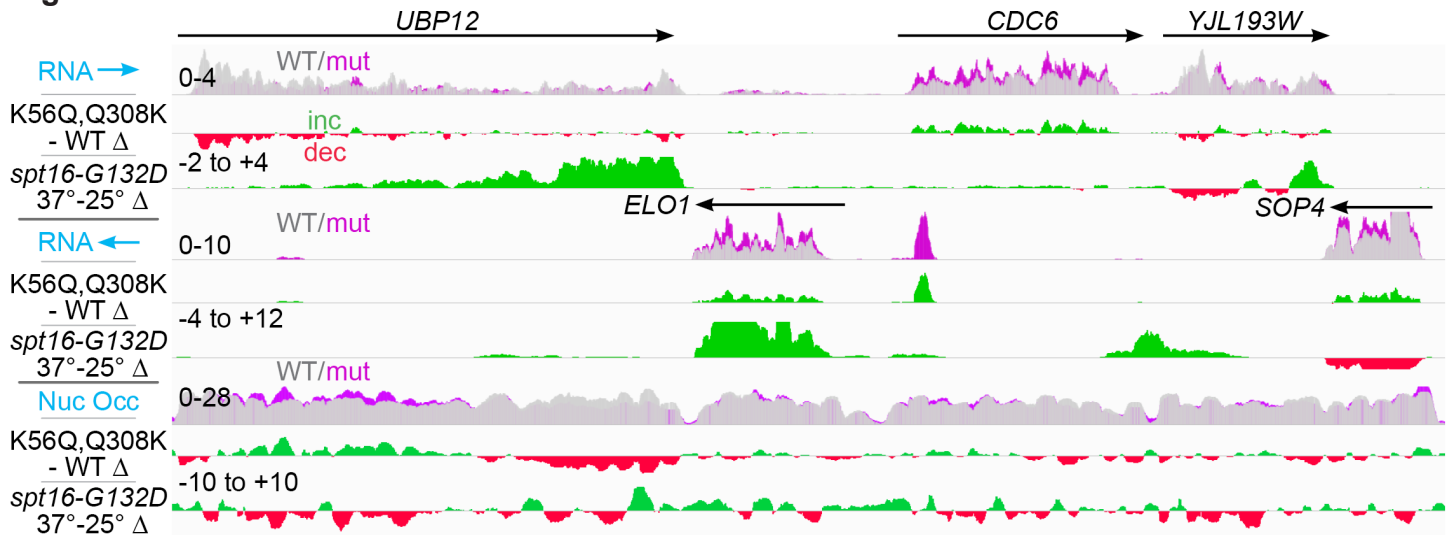
Fig 5SI. Effects of the orientation of the downstream neighbor on 3' end nucleosome occupancy

Nucleosome occupancy profiles were aligned by the terminal nucleosome for 5545 genes as in Fig 5D (black line). 3922 of these were readily oriented relative to the neighboring gene downstream, and this subset did not have a different nucleosome occupancy profile than the larger group (dotted line). When separated into genes with downstream neighbors transcribed in the same direction as the target gene (the downstream region is the promoter for the neighbor) and those with converging transcription (the downstream region is the termination site for both genes), distinctive patterns were observed. Target genes whose 3' end contained the promoter of the downstream neighbor had higher occupancy of the terminal nucleosome, and lower occupancy downstream (green compared to blue lines). This is consistent with a promoter/NDR in this region, possibly leading to enhanced positioning of the sentinel -1 nucleosome for that promoter/the terminal nucleosome of the target gene. These patterns were retained in mutants, albeit with lower overall occupancy as noted in Fig 5C (right panel; only the more severe combined mutant is shown).

Fig 6S**Fig 6S.** Browser tracks illustrating features of chromatin and expression changes revealed by global analysis.

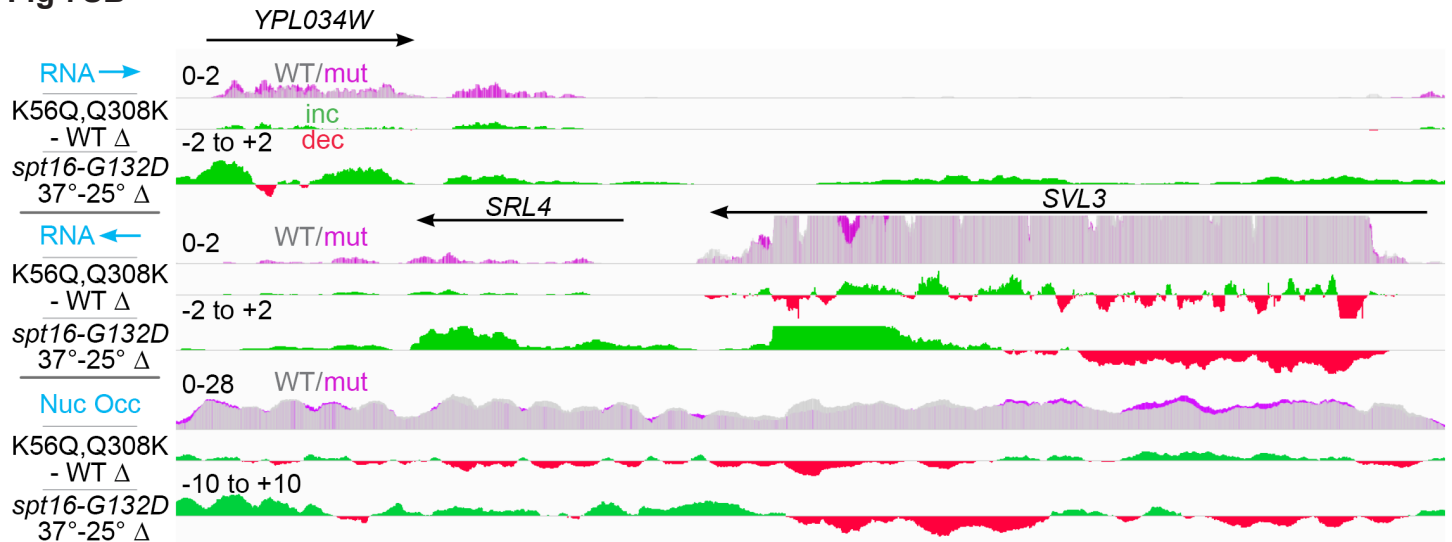
Bigwig tracks were loaded into the Integrative Genomics Viewer (IGV, ROBINSON *et al.* 2011; THORVALDSDOTTIR *et al.* 2013). 12 kb of the region near *CHA1* are shown. The top three tracks show forward RNA reads, with the top track showing the values for the WT strain (gray) overlaid over the values for the H3-K56Q *pob3-Q308K* strain (magenta). The location of each annotated gene oriented in the forward direction is indicated. The second track shows the difference between the WT and mutant values with green signals indicating increased transcript levels in the mutant and red indicating a decrease in the mutant. The third track shows a similar difference map comparing the values obtained with the *spt16-G132D* mutant after a 45-minute incubation at 37° relative to the same strain prior to inactivation of FACT, using data published in GSE66215 (FENG *et al.* 2016). These tracks therefore show the relative transcript levels in our WT and mutant strains, the change in this combined mutant strain, and the same information for acute withdrawal of FACT. The next three tracks are the same as above except for RNA representing the reverse strand, and the bottom three tracks are the same as above except they show nucleosome occupancy revealed by MNase-seq. Numbers indicate the range of values plotted.

Transcription of *CHA1* is typically repressed unless serine or threonine are the sole nitrogen source available (PETERSEN *et al.* 1988). This is not the case for the datasets shown, so the WT strain produced few transcripts. In both cases, the mutant strains failed to maintain repression, leading to increased transcript levels, with a more dramatic increase after acute withdrawal of FACT. Increased transcript accumulation was associated with noticeable loss of nucleosome occupancy over the gene body after acute FACT withdrawal, but the H3-K56Q *pob3-Q308K* strain displayed little change in nucleosome positioning and a small increase in occupancy. *MRC1* displayed signs of strong nucleosome occupancy loss throughout the gene and potential activation of a cryptic bidirectional promoter, as transcript accumulation was enhanced in both directions beginning in the middle of the gene. No similar effect was observed in our data, indicating different effects of the chronic and acute FACT defects. As with *CHA1*, *PRD1* also displayed increased transcript accumulation in the H3-K56Q *pob3-Q308K* mutant, and again this was associated with an increase in nucleosome occupancy over the 5' region of the gene and its promoter, in contrast to the expectation that elevated nucleosome occupancy would cause decreased transcription. *KRR1* displayed mixed effects on nucleosome occupancy, but each of the other genes displayed the decrease observed in the global analysis in Figs 5B, 5D, 5SE, and 5SH.

Fig 7SA**Fig 7SA, 7SB. Browser tracks illustrating different classes of antisense effects**

Tracks are as described in Fig 6SB. (A) ~10 kb near the *CDC6* locus. This gene displays a large increase in antisense transcript signal centered over the +2 nucleosome (note that the forward RNA track is displayed on a scale from 0 to 4 whereas the reverse track is 0 to 10 to allow the effect to be fully observed). While antisense transcript signal is significant from this region out through the promoter of *CDC6*, it diminishes near the edge of the +1 nucleosome, without any notable change in the occupancy or positioning of either nucleosome, and a slight increase in the +3 nucleosome where the antisense transcription presumably initiates. Sense transcript accumulation is overall increased, indicating that the antisense transcription does not block use of the *CDC6* promoter. Acute loss of FACT had a quantitatively and qualitatively different effect, but instead caused a strong antisense signal downstream of *CDC6*, apparently initiating in the neighboring gene *YJL193W*, without strongly affecting overall transcription from this gene (although possibly activating a bidirectional cryptic promoter). All 5 genes shown display the pattern of 3' end nucleosome loss, while this is less apparent after acute withdrawal of FACT.

(B) Tracks are the same as above, except 5.6 kb near *SRL4* are shown. The forward and reverse RNA tracks are shown on the same scale to highlight the increase in both sets of signals for this gene, with greater antisense than sense transcript levels. In this case, the antisense transcription occurs across the gene body, rather than at the 5' end. Acute loss of FACT causes a similar, but larger, effect on both sense and antisense transcript accumulation, but the two strains show opposite effects on nucleosome occupancy (decreased in H3-K56Q *pob3-Q308K*, increased in *spt16-G132D* at 37°). *SVL3* again illustrates the 3' end nucleosome depopulation observed in our mutants, distinct from the pattern caused by acute FACT withdrawal.

Fig 7SB

Supplementary Methods

RNA-seq: Three independent cultures for each genotype (Table S1) were grown to an OD of about 0.7 in rich medium at 30°, harvested by centrifugation, and frozen in liquid nitrogen. RNA was extracted with 0.5% SDS and phenol at pH 4.3 at 65° for one hour, pelleted in 5.7 M cesium chloride, then purified using Qiagen RNeasy Mini kits according to the manufacturer's instructions. Libraries were prepared with NEBNext Directional RNA Library kits followed by Illumina Ribo-Zero Gold kits, and sequenced using the Illumina HiSeq 50 single-read protocol.

Reads were aligned to the yeast genome (version R64 or SacCer3) using Novoalign (version 2.8, <http://www.novocraft.com/products/novoalign/>) with an index containing splice junctions prepared with USeq MakeTranscriptome (<https://github.com/HuntsmanCancerInstitute/USeq>). Alignments to splice junctions were converted to genomic alignments with USeq SamTranscriptomeParser (release 9.1.3), allowing for only 1 multi-mapper randomly assigned. Counts and TPM values were generated using the BioToolBox (version 1.53, <https://github.com/tiparnell/biotoolbox>) get_datasets script, restricting as necessary by strand, relative coordinates, and/or percentage of transcript length. Differential expression was performed with DESeq2 (version 1.16; Love *et al.* 2014). All samples were loaded into a DESeq2 matrix and individual contrasts were applied for each genotype versus WT; log₂ fold changes were reported as shrunken values using the *lfcShrink* function. Genes were selected for significance based on both adjusted P-value (< 0.01) and log₂ fold change (absolute > 1). For plot generation, regularized log₂ (rlog₂) counts were generated using DESeq2. To remove slow-growth signatures, the rlog₂ values were processed using the R script described (O'Duibhir *et al.* 2014).

For spatial analysis, RNA-seq coverage files were generated with BioToolBox bam2wig using RPM (Reads Per Million) depth scaling and averaging the depth-normalized coverage among the biological replicates. For convenient plotting, this data was then log₂ transformed using BioToolBox manipulate_wig. Data was collected as the mean coverage depth in windows across regions of interest such as average length gene (BioToolBox script get_binned_data) or around promoters or 3' ends of genes (BioToolBox script get_relative_data).

MNase-seq: Three independent cultures for each genotype (Table S1) were grown as above to an OD of about 0.8, then formaldehyde was added to a final concentration of 1% and the samples were shaken at RT for 20 minutes. Glycine was added to 0.2 M, then cells were harvested, washed twice, then frozen in liquid nitrogen. Cell walls were removed with lyticase (Sigma-Aldrich), spheroplasts were lysed in 1% Triton X-100, and chromatin was digested with MNase (Worthington) after testing titrations to determine the optimal level of digestion. After reversing crosslinks for 5 hours at 65°, DNA was recovered by ethanol precipitation, treated with RNase A and Proteinase K (NEB) and purified on Qiaquick PCR Purification kits (Qiagen). Libraries were prepared with NEBNext ChIP-Seq kits, then the ~270 bp band was purified by agarose gel electrophoresis followed by extraction using MinElute Gel Extraction kits (Qiagen) and sequencing by the Illumina HiSeq 50 single-read method.

Reads were aligned to the genome using Novoalign (version 2.8), allowing for zero multi-mapping alignments and filtering for a mapping quality > 13. Samples had about 50-60% duplication rates. To reduce and normalize duplicate reads while maintaining biological enrichment, duplicate reads were randomly subsampled to a uniform rate of 40% using the bam_partial_dedup application (version 1.7, <https://github.com/HuntsmanCancerInstitute/MultiRepMacsChIPSeq>). Normalized fragment coverage tracks were generated using BioToolBox bam2wig, extending the fragment to 150 bp, and RPM depth-normalization. To compare biological replicates, the mean fragment coverage was collected in windows of 10 or 25 bp across the genome for each separate replicate, restricted to promoter regions (-400 to +800), and PCA plots were generated with R. For subsequent analysis, biological replicates were RPM normalized and averaged.

Nucleosome profiles were collected using the BioToolBox program get_relative_data as described above. To identify and map nucleosome positions, scripts used in the package <https://github.com/tiparnell/biotoolbox-nucleosome> were utilized. As input data, nucleosome fragment midpoint occupancy was generated with BioToolBox bam2wig, recording start positions shifted downstream by 74 bp with RPM normalization and averaging between replicates. Nucleosomes were called with map_nucleosomes.pl using a threshold of 0.2. Nucleosome mappings were re-verified with verify_nucleosome_mapping.pl, filtering overlapping nucleosomes with maximum overlap of 35 bp and re-centering enabled (the majority of overlapping nucleosomes are in ambiguous areas with poor phasing, usually in the middle of long genes). This identified 62,083 nucleosomes in the WT genome. Nucleosomes were assigned to relative genic positions (-1, +1, +2, +3, and +4) with the script in the yeast_positioned_nucleosomes subfolder in the BioToolBox-nucleosome package. To correlate shift positions, the BioToolBox application correlate_position_data was used with the mapped genic nucleosomes with a radius of 50 bp from the midpoint and "skinny" nucleosome fragment coverage files. The skinny nucleosome fragment coverage was prepared using BioToolBox bam2wig with a shift value of 37 bp and extension of 75 bp, essentially recording the middle 50% of the predicted fragment to accentuate the core occupancy of the nucleosome.

Supplementary References

- Feng, J., H. Gan, M. L. Eaton, H. Zhou, S. Li *et al.*, 2016 Noncoding Transcription Is a Driving Force for Nucleosome Instability in *spt16* Mutant Cells. *Mol Cell Biol* 36: 1856-1867.
- Love, M. I., W. Huber and S. Anders, 2014 Moderated estimation of fold change and dispersion for RNA-seq data with DESeq2. *Genome Biol* 15: 550.
- Marquardt, S., R. Escalante-Chong, N. Pho, J. Wang, L. S. Churchman *et al.*, 2014 A chromatin-based mechanism for limiting divergent noncoding transcription. *Cell* 157: 1712-1723.
- McCullough, L., Z. Connell, C. Petersen and T. Formosa, 2015 The Abundant Histone Chaperones Spt6 and FACT Collaborate to Assemble, Inspect, and Maintain Chromatin Structure in *Saccharomyces cerevisiae*. *Genetics* 201: 1031-1045.
- McCullough, L., B. Poe, Z. Connell, H. Xin and T. Formosa, 2013 The FACT histone chaperone guides histone H4 into its nucleosomal conformation in *Saccharomyces cerevisiae*. *Genetics* 195: 101-113.
- O'Duibhir, E., P. Lijnzaad, J. J. Benschop, T. L. Lenstra, D. van Leenen *et al.*, 2014 Cell cycle population effects in perturbation studies. *Mol Syst Biol* 10: 732.
- Pelechano, V., S. Chavez and J. E. Perez-Ortin, 2010 A complete set of nascent transcription rates for yeast genes. *PLoS One* 5: e15442.
- Petersen, J. G., M. C. Kielland-Brandt, T. Nilsson-Tillgren, C. Bornaes and S. Holmberg, 1988 Molecular genetics of serine and threonine catabolism in *Saccharomyces cerevisiae*. *Genetics* 119: 527-534.
- Robinson, J. T., H. Thorvaldsdottir, W. Winckler, M. Guttman, E. S. Lander *et al.*, 2011 Integrative genomics viewer. *Nat Biotechnol* 29: 24-26.
- Sun, M., B. Schwalb, N. Pirkl, K. C. Maier, A. Schenk *et al.*, 2013 Global analysis of eukaryotic mRNA degradation reveals Xrn1-dependent buffering of transcript levels. *Mol Cell* 52: 52-62.
- Thorvaldsdottir, H., J. T. Robinson and J. P. Mesirov, 2013 Integrative Genomics Viewer (IGV): high-performance genomics data visualization and exploration. *Brief Bioinform* 14: 178-192.
- Xin, H., S. Takahata, M. Blanksma, L. McCullough, D. J. Stillman *et al.*, 2009 yFACT induces global accessibility of nucleosomal DNA without H2A-H2B displacement. *Mol Cell* 35: 365-376.